CHEMISTRY

Charge-clustering induced fast ion conduction in 2LiX-GaF₃: A strategy for electrolyte design

Sawankumar V. Patel[1,2]†, Valentina Lacivita[3]†, Haoyu Liu[1]†‡, Erica Truong[1], Yongkang Jin[1], Eric Wang[3], Lincoln Miara[3]§, Ryounghee Kim[4], Hyeokjo Gwon[4], Rongfu Zhang[1,2], Ivan Hung[2], Zhehong Gan[2], Sung-Kyun Jung[4,5]*, Yan-Yan Hu[1,2]*

2LiX-GaF₃ (X = Cl, Br, I) electrolytes offer favorable features for solid-state batteries: mechanical pliability and high conductivities. However, understanding the origin of fast ion transport in 2LiX-GaF₃ has been challenging. The ionic conductivity order of 2LiCl-GaF₃ (3.20 mS/cm) > 2LiBr-GaF₃ (0.84 mS/cm) > 2LiI-GaF₃ (0.03 mS/cm) contradicts binary LiCl (10^{-12} S/cm) < LiBr (10^{-10} S/cm) < LiI (10^{-7} S/cm). Using multinuclear ^{7}Li, ^{71}Ga, ^{19}F solid-state nuclear magnetic resonance and density functional theory simulations, we found that Ga(F,X)$_n$ polyanions boost Li⁺-ion transport by weakening Li⁺-X⁻ interactions via charge clustering. In 2LiBr-GaF₃ and 2LiI-GaF₃, Ga-X coordination is reduced with decreased F participation, compared to 2LiCl-GaF₃. These insights will inform electrolyte design based on charge clustering, applicable to various ion conductors. This strategy could prove effective for producing highly conductive multivalent cation conductors such as Ca²⁺ and Mg²⁺, as charge clustering of carboxylates in proteins is found to decrease their binding to Ca²⁺ and Mg²⁺.

INTRODUCTION

High-performance inorganic solid electrolytes are indisputably crucial to the transition of current rechargeable Li⁺-ion batteries that use liquid electrolytes to all-solid-state batteries (ASSBs) for both enhanced safety and high energy density. A repertoire of properties has been considered to design solid electrolyte for successful integration in ASSBs, namely, ionic conductivity, air/water stability, electrode compatibility over extended temperature and voltage range, and mechanical pliability. Various solid electrolytes have been developed in attempts to satisfy those criteria (1–4). Superionic conductors with conductivities on the order of ~10 mS/cm, even surpassing the ionic conductivity of state-of-the-art liquid electrolytes, have been developed in sulfide-based chemical spaces. Prominent examples of these materials are argyrodite and thio-LISICON electrolytes (5–11). Chemical stability against both Li metal and air exposure has also been achieved in oxide-based solid electrolytes, such as garnets (12). Other solid electrolytes such as hydrides or halides present excellent reduction and oxidation stability, respectively (13).

Currently, a core issue of ASSBs is the mechanical, chemical, and electrochemical compatibility of solid electrolytes with electrodes (14–16). Nonconformal contact at the electrode-electrolyte interface limits the power density and induces dendrite formation in ASSBs (17). Most sulfide, oxide, halide solid electrolytes often need a high stack pressure (a few megapascals) or a cosintering process for ASSB fabrication and operation (18, 19). However, these strategies seem inadequate to maintain physical integrity given the reversible volume change of electrodes upon electrochemical cycling (19). Therefore, to avoid dynamic mechanical degradation, the design of high-performance solid electrolytes should also take into account physical deformability, which is required to accommodate stress and strain evolution at the interface (16, 20–22).

Recently developed Ga-based mixed-halide solid electrolytes could be a valuable venue to address the interface issues due to promising characteristics including high ionic conductivity and physical pliability (23). These materials exhibit high ionic conductivity over 3 mS/cm and clay-like mechanical properties, corresponding to complex shear moduli of 10^5 to 10^6 Pa, which enable the ASSBs to operate without stack pressure to maintain conformal cathode-electrolyte interface contact over extended stable electrochemical cycling. Although it is vaguely understood from the synthesis perspective that the unique features of these solid electrolytes can be observed only when mixed halide anions are incorporated, their amorphous structure with the absence of long-range ordering makes it challenging to trace the structural origin of fast ion transport.

Here, to elucidate the short-range structures in clay-like solid electrolytes and their correlation with the ion transport, we have performed combined analyses using x-ray diffraction (XRD), solid-state nuclear magnetic resonance (NMR), and density functional theory (DFT) calculations on systems with reference stoichiometry 2LiX-GaF₃ (X = Cl, Br, I). We reveal that the identity of X anions has a substantial effect on the observed Li⁺-ion conductivity. The conductivity is 3.2 mS/cm when X = Cl and is reduced by a factor ~ 4 for X = Br (8.39×10^{-1} mS/cm) and by about 100 times for X = I (3.04×10^{-2} mS/cm). We have identified the formation of complex GaCl$_m$F$_{n-m}$ polyanions in 2LiCl-GaF₃, and consequent diversification of the Li⁺ local environments, as a major factor

in promoting fast ion transport by limiting strong Li-F ionic interactions that can slow down Li$^+$ transport. More generally, in drawing a parallel with the concept of "charge clustering" well known in biochemistry (24), the Ga(X,F)$_n$ polyanions forming the 2LiX-GaF$_3$ amorphous framework may be conceived as gallium-centered clusters where multiple negatively charged anions (F$^-$ and X$^-$ halides) are attracted to a central gallium cation. Such negative charge clustering in gallium-based polyanions screens interactions between positive charge carriers and negative hosts, therefore weakening Li$^+$ binding affinity for fast ion transport. In contrast, Br and I tend to displace F from its interactions with Ga, thus limiting the charge clustering screening effect on the Li$^+$-ion conduction. This study enriches our understanding of amorphous solid electrolytes and provides further insight for designing highly conductive clay-like ion conductors.

RESULTS

The amorphous character of 2LiX-GaF$_3$

X-ray powder diffraction was used to identify crystalline phases present in the 2LiX-GaF$_3$ (X = Cl, Br, I) samples. Figure 1A compares powder x-ray patterns of the 2LiX-GaF$_3$ compounds and the precursor GaF$_3$. All three mixed halide compositions display only weak crystalline peaks that are largely overridden by a broad, dominant background, revealing that the major phases are highly disordered. The absence of Bragg peaks from precursors GaF$_3$ and LiX also indicates that chemical reactions have taken place to transform them into new phases. An attempt to match the weak Bragg peaks in 2LiX-GaF$_3$ was conducted by performing a search match with the available phases in the Inorganic Crystal Structure Database (ICSD)

as shown in Fig. 1 (B to D). The phases that matched with the weak crystalline peaks in 2LiCl-GaF$_3$ are Li$_3$GaF$_6$ (ICSD ID: 409384) and LiGaCl$_4$ (ICSD ID: 60849). In 2LiBr-GaF$_3$ and 2LiI-GaF$_3$, the diffraction peaks matched LiGaBr$_4$ (ICSD ID: 61337) and LiGaI$_4$ (ICSD ID: 60850), respectively. The abovementioned crystalline peaks may hint at the presence of local structures having characteristics similar to the Li$_3$GaF$_6$ and LiGaX$_4$ (X = Cl, Br, I) structures. However, because of poor crystallinity of the 2LiX-GaF$_3$ samples, powder XRD was insufficient to provide more detailed phase or structure information.

Ionic conductivities dependent on halide-anion species

The ionic conductivities of 2LiX-GaF$_3$ (X = Cl, Br, I) samples determined via variable-temperature electrochemical impedance spectroscopy (EIS) are shown in Fig. 2. All samples exhibit a curvature in the $\log_{10}(\sigma)$ versus $1/T$ plot showing a deviation from the Arrhenius behavior. This deviation from Arrhenius behavior is typically observed in glass and polymer-based solid electrolytes (25–27).

Overall, at 25°C, 2LiCl-GaF$_3$ has the highest ionic conductivity of 3.2 mS/cm among the three. The ionic conductivity drops upon Cl$^-$ substitution with Br$^-$ (8.39×10^{-1} mS/cm) and is the lowest with I$^-$ (3.04×10^{-2} mS/cm). The crystalline phases observed using XRD (Fig. 1), such as Li$_3$GaF$_6$ and LiGaX$_4$, have poor ionic conductivity (28–30). Therefore, the difference in ionic conductivities of 2LiX-GaF$_3$ (X = Cl, Br, I) implies that the presence of mixed-halide anion species affects the local structure and energy landscape for Li$^+$-ion transport.
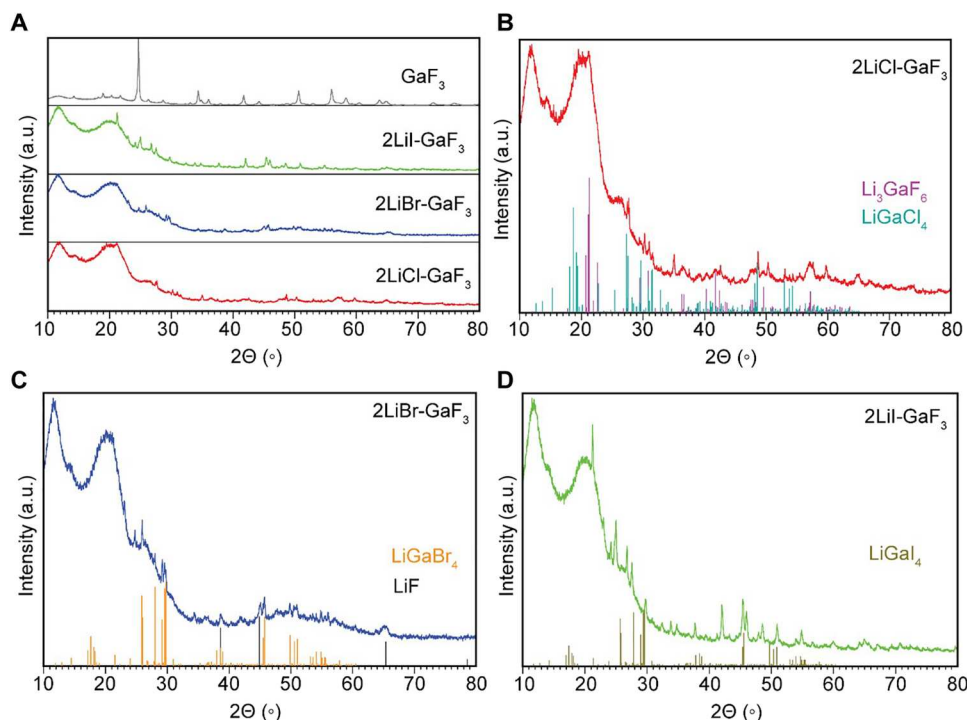
Fig. 1. Analysis of crystalline phases formed in 2LiX-GaF$_3$ (X = Cl, Br, I) via powder x-ray diffraction. (**A**) An overview of the pXRD patterns of 2LiX-GaF$_3$ and GaF$_3$. Identification of minor crystalline phases in (**B**) 2LiCl-GaF$_3$, (**C**) 2LiBr-GaF$_3$, and (**D**) 2LiI-GaF$_3$, based on the ICSD database. a.u., arbitrary units.
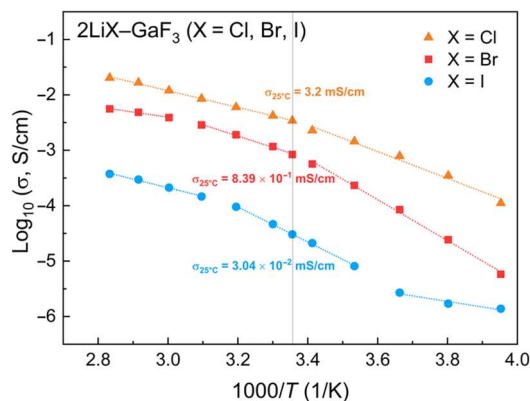
Fig. 2. Ionic conductivities of 2LiX–GaF₃ (X = Cl, Br, I) electrolytes. Measurements were determined using AC EIS.

Local structures of 2LiX-GaF₃ (X = Cl, Br, I)

Solid-state NMR is a powerful tool for characterizing local structures of highly disordered materials. A combination of multinuclear ^{71}Ga, ^{19}F, and ^{7}Li NMR, along with DFT-generated amorphous models, was used to investigate local structures in the 2LiX-GaF₃ compounds.

1) The gallium environment

High-resolution ^{71}Ga NMR was collected to probe the local environment of Ga. ^{71}Ga is an NMR-active quadrupole (spin-3/2) nucleus, therefore the electric field gradient around the Ga ions is highly sensitive to its local structural environment. To ensure broadband excitation, a Quadrupolar Carr-Purcell Meiboom-Gill (QCPMG) pulse sequence was used to acquire ^{71}Ga NMR spectra, which are shown in Fig. 3A. QCPMG NMR yields a series of evenly spaced spikelets, the skyline of which formulates the NMR peak shape.

The chemical shift of Ga in oxidation state +3 generally ranges from 700 to 0 ppm, whereas Ga in oxidation state +1 ranges from 0 to −700 ppm (31–33). Because the ^{71}Ga peaks of 2LiX-GaF₃ (X = Cl, Br) spread through positive chemical shift ranges, we conclude that most of the gallium in 2LiX-GaF₃ (X = Cl, Br) exists in oxidation state +3. In 2LiI-GaF₃, the ^{71}Ga NMR shows the largest bandwidth spanning from −250 to 300 ppm, which hints the existence of gallium in mixed oxidation states of +3, +2, and +1.

The broadening of the main ^{71}Ga NMR resonance (Fig. 3A) indicates that gallium exists in a disordered environment. The parameters used to fit these ^{71}Ga NMR resonances are presented in Table 1. A large quadrupole coupling constant (C_q) value of >8 MHz is found. The Ga peak shifts toward lower ppm in *2LiX-GaF₃* from X = Cl to Br and I. This is in agreement with literature reports where Ga coordinated by I⁻ shows upfield shift compared to Ga coordinated by Cl⁻ and Br⁻ anions (34–36). The different anion electronegativities may account for the differences in chemical shift. An additional small symmetric peak is observed around 40 ppm in the 2LiCl-GaF₃ phase. Such a peak is attributed to the crystalline Li₃GaF₆ phase that is also evident in powder XRD (Fig. 1). The other crystalline phases identified from the XRD pattern, i.e., LiGaX₄ (X = Cl, Br, I), may be hidden underneath the main broad ^{71}Ga band.

Further insight into the Ga coordination environment is provided by DFT simulations. An example of amorphous structure model obtained by ab initio molecular dynamics (AIMD) simulated annealing for 2LiCl-GaF₃ is presented in Fig. 3B. Figure 3C illustrates the statistical distribution of X and F anions around Ga in the amorphous structure models generated for the different 2LiX-GaF₃ (X = Cl, Br, I) compositions. All structures contain mixed GaX_mF_{n-m} polyanions with the numbers m and $(n − m)$ of X and F ligands being negatively correlated. Ga is found in highly diverse coordination environments. Ga^{3+} is coordinated by X and F anions in tetrahedral (IV, $n = 4$), pentahedral (V, $n = 5$), and octahedral (VI, $n = 6$) forms. Because of large quadrupolar couplings in all such environments, as expected from NMR data on reference Ga oxides (C_q up to ~17 MHz) (37), the resonance of Ga^{3+} in (IV) versus (V) coordination is not distinguishable in the ^{71}Ga NMR spectra, therefore Ga (IV) and (V) are referred to as a single complex anion.

C_q and asymmetry parameters of Ga in the simulated 2LiX-GaF₃ (X = Cl, Br, I) amorphous structures were calculated by DFT NMR. The results are reported in Table 1 and in table S1. A large C_q of >8 MHz is calculated for most Ga^{3+}. Comparisons between Ga coordination environments in the DFT simulated amorphous structures for 2LiCl-GaF₃, 2LiBr-GaF₃, and 2LiI-GaF₃ (Fig. 3C) also reveal a somewhat greater variety of mixed GaX_mF_{n-m} polyanions, in terms of the numbers m and $(n − m)$ of X and F anions coordinating Ga, in the chlorine-based compound than in the bromine and iodine ones. That is, while in simulated 2LiCl-GaF₃ amorphous structures Ga shows a high likelihood of forming complex mixed GaX_mF_{n-m} polyanions with $n = 4, 5, 6$ and $m = 1, 2, 3$, a somewhat more homogeneous Ga coordination by X and F is found in the amorphous models of 2LiBr-GaF₃ ($n ≈ 5$, $m ≈ 2$), and of 2LiI-GaF₃, where $n ≈ 4$ and $m ≈ 2$ to 3.

Some amorphous structure models are further characterized by the presence of direct Ga-Ga interactions (bond length $d_{Ga-Ga} ≈$ 2.45 Å) forming dimeric $Ga_2(X,F)_6$ units typical of Ga^{2+} compounds such as GaS (ICSD ID: 25660). In particular, $Ga_2(X,F)_6$ dimers involve a significant amount (up to about 20%) of Ga atoms in 2LiI-GaF₃, whereas they only account for less than 10% of Ga in the other compositions. Lastly, a small portion of Ga (~3%) in simulated amorphous 2LiI-GaF₃ is not covalently bonded into any molecular species, the distance from the nearest I⁻ and F⁻ anions ($d_{Ga-I} ≈ 3.3$ Å, $d_{Ga-F} ≈ 2.7$ Å) being far larger than the sum of the corresponding ionic radii (i.e., 2.8 and 1.9 Å, respectively), as shown by the pair distribution functions in fig. S1. Interaction distances $d_{Ga-I} > 3$ Å are comparable to those occurring around Ga^{1+} in GaI₂ (ICSD ID: 24821). Therefore, we assign formal oxidation state +1 to such noncovalently bonded Ga species. Indeed, the associated Bader charge is ~0.6 |e⁻|, much lower than the average Ga charge calculated for 2LiI-GaF₃, i.e., ~1.4 |e⁻|. It is noteworthy that the presence of Ga^{2+} and of Ga^{1+}, albeit minor, in 2LiI-GaF₃ is consistent with both the broadening and upfield shift of the ^{71}Ga NMR signal observed for 2LiI-GaF₃ (Fig. 3A).

2) The fluorine environment

Further structural insights into 2LiX-GaF₃ (X = Cl, Br, I) are obtained by analyzing the local fluorine chemical environment using ^{19}F NMR. Figure 4A shows the ^{19}F NMR spectra. Solid GaF₃ (shown in blue at the top) resonates at −170 ppm with a shoulder to the left of the GaF₃ resonance that may be from the hydrated forms. ^{19}F NMR of 2LiX-GaF₃ (X = Cl, Br, I) was performed under static conditions due to difficulties in spinning the samples.
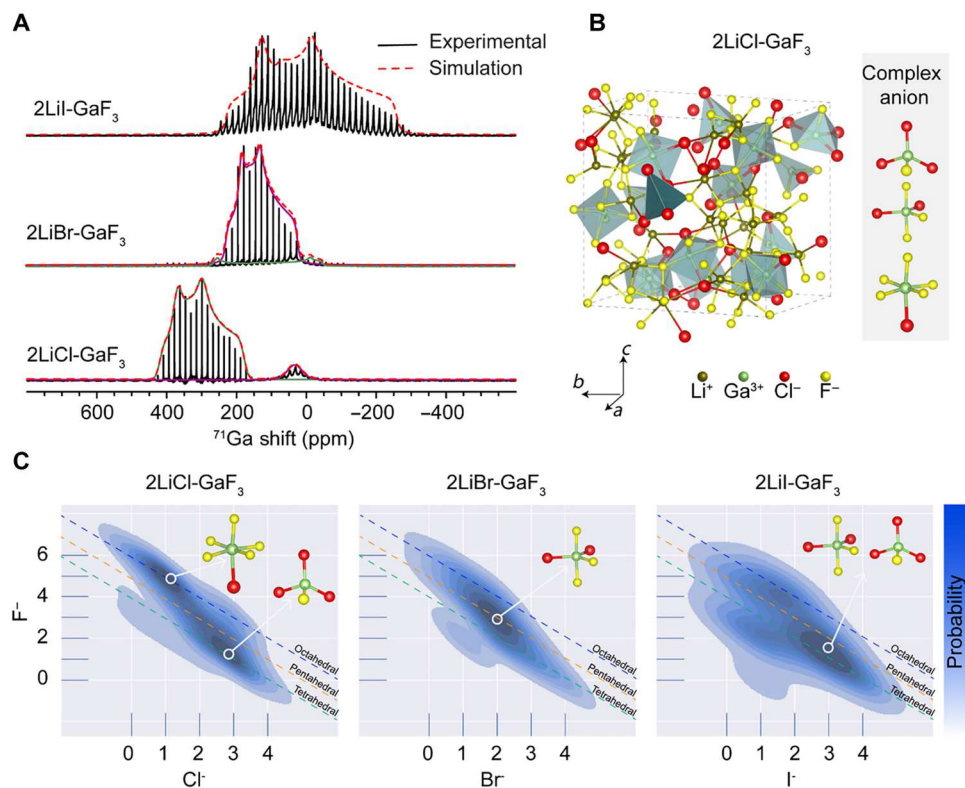
Fig. 3. Ga coordination environment examined with ^{71}Ga NMR and AIMD simulations. (**A**) Static QCPMG ^{71}Ga NMR spectra of 2LiX-GaF$_3$ (X = Cl, Br, I) and corresponding spectral fits. The resulting quadrupolar coupling constants and asymmetry parameters are documented in Table 1. (**B**) Simulated amorphous structure of 2LiCl-GaF$_3$ showing gallium coordinated with fluorine and chlorine to form complex anions GaCl$_m$F$_{n-m}$. (**C**) Statistical distribution of F and X anions coordinating Ga in the amorphous structural models for 2LiX-GaF$_3$, generated with AIMD simulated annealing. Among the most probable complex anions are GaCl$_1$F$_5$, GaCl$_3$F$_1$, GaBr$_2$F$_3$, and GaI$_3$F$_1$.

All spectra display multiple resonances signifying complex structural heterogeneity in the mixed-anion compounds. A broad peak is observed in all three samples, assigned to F coordinated in complex Ga(X, F)$_n$ polyanion species, i.e., clustered F$^-$, as shown in Fig. 3B. In agreement with the experimental observation, Fig. 4B shows that DFT-computed ^{19}F chemical shifts for the amorphous model structure of 2LiCl-GaF$_3$ yield a similar broad peak spanning between −75 and − 250 ppm. While this chemical shift range covers most of the experimental ^{19}F NMR resonances, we notice that a small portion (less than 10% of the overall intensity) of the measured spectra extends further to 0 ppm. Such a discrepancy may be explained by the limited size (120 atoms) and, consequently, statistical representativity of our model, as well as by the absence, from the simulations, of broadening factors common to experimental NMR, such as thermal effects, orientation anisotropy in sample powders, dipolar couplings, etc.

Quantification of the resonances from ^{19}F NMR is presented in Fig. 4C. Upon replacement of Cl$^-$ with Br$^-$ and with I$^-$, the intensity of the complex anion resonance decreases, whereas a new sharp resonance appears at ≈−129 to −133 ppm in the 2LiBr-GaF$_3$ and 2LiI-GaF$_3$ samples, respectively. The sharp resonance is attributed to single "mobile" F$^-$ anions. Because the NMR spectra were collected under static conditions, homonuclear dipolar interactions dominate the line broadening in ^{19}F NMR. Therefore, a narrow line shape is indicative of weaker dipolar interactions which may be

related to F$^-$ species with high mobility. A survey of ^{19}F-NMR data on F$^-$-ion conductors demonstrates resemblance in line shape width (<1 kHz) (38–40). Therefore, the overall ionic conductivities measured for 2LiBr-GaF$_3$ and 2LiI-GaF$_3$ may contain contributions from both Li$^+$ and F$^-$ ion transport. The Li$^+$ conduction in 2LiBr-GaF$_3$ and 2LiI-GaF$_3$ may be even more strongly hindered than the apparent ionic conductivities suggest.

Residual sharp peaks, which we label as "unknown" species in Fig. 4C, may possibly be attributed to the minor crystal phases that matched in powder XRD (Fig. 1). In the case of 2LiCl-GaF$_3$, crystalline Li$_3$GaF$_6$ is a probable phase at −161 ppm. In the case of 2LiBr-GaF$_3$ and 2LiI-GaF$_3$, the unknown peaks reside at −129 ppm. Those peaks remain unassigned, but we hypothesize contributions from mono-anion species similar to HF, the chemical shift of which varies between −140 and −160 ppm (41).

3) The lithium environment

In addition, ^{7}Li NMR was used to probe the Li$^+$-ion environment. In all three compositions, a broad and a narrow resonance of ^{7}Li are observed, as shown in Fig. 5A. The sharp Lorentzian peak shape is typical of Li ions in fast ion conductors, whereas the broad Gaussian peak shape often represents Li ions with low mobility in anisotropic environments (42, 43). Therefore, we attribute the broad resonance to a slow-moving Li component and the sharp resonance to a fast-moving Li component. Quantification of the broad and sharp components in the three compositions is presented in Fig. 5B. The
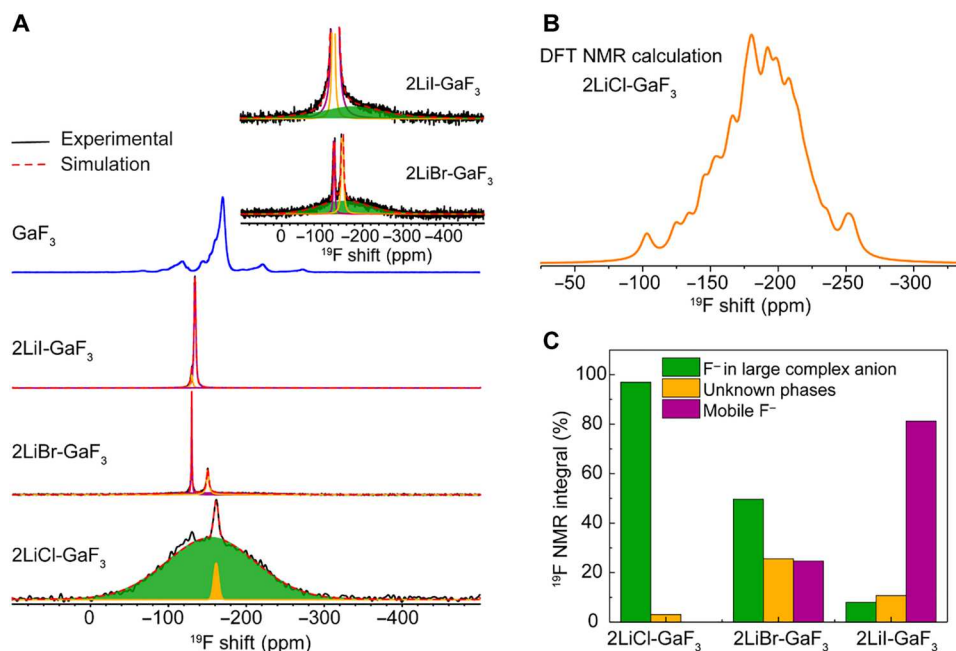
Fig. 4. Quantification of F⁻ integrated into complex GaX$_m$F$_{n-m}$ anions in 2LiX-GaF$_3$ (X = Cl, Br, I) with ¹⁹F NMR. (**A**) Static ¹⁹F NMR spectra of 2LiX-GaF$_3$ (X = Cl, Br, I). The broad Gaussian peak comes from complex GaX$_m$F$_{n-m}$ anions with limited mobility. The sharp NMR resonances are from highly mobile F⁻ ions. (**B**) DFT calculated ¹⁹F NMR based on the amorphous structure model for 2LiCl-GaF$_3$ as shown in Fig. 3B. (**C**) Quantification of F in different chemical environments based on ¹⁹F NMR in (A).

composition 2LiCl-GaF$_3$ displays the largest fraction of fast-moving Li⁺, in agreement with it having the highest measured ionic conductivity.

Figure 5C provides a statistical analysis of the Li⁺ environments observed in the amorphous structure models generated with AIMD-simulated annealing for 2LiX-GaF$_3$ (X = Cl, Br, I). We notice that for X = Cl, the Li⁺ coordination environment is somewhat diversified, including both tetrahedral and pentahedral local structures, whereas for X = Br, I, the Li⁺ is found mainly in tetrahedral coordination. Furthermore, the affinity of the X anions toward Li⁺ decreases from X = Cl⁻, to Br⁻, and to I⁻. As indicated by the maxima in the probability distribution highlighted in Fig. 5C, the average number of X⁻ anions around Li⁺ diminishes from being approximately 2 for X = Cl, to 0 to 1 for X = Br and to 0 for X = I, while the relative amount of F⁻ increases. In drawing a parallel with the two Li⁺ components detected in the ⁷Li NMR (Fig. 4A), we might associate the broad peak that prevails in 2LiI-GaF$_3$ to Li⁺ ions mainly involved in strong interactions with the highly electronegative F⁻, whereas the sharp Lorentzian peak of the fast-moving Li component, that is most abundant in 2LiCl-GaF$_3$, might be attributed to Li⁺ ions contended with GaX$_m$F$_{n-m}$ ($n - m > 0$, $m > 0$) polyanions.
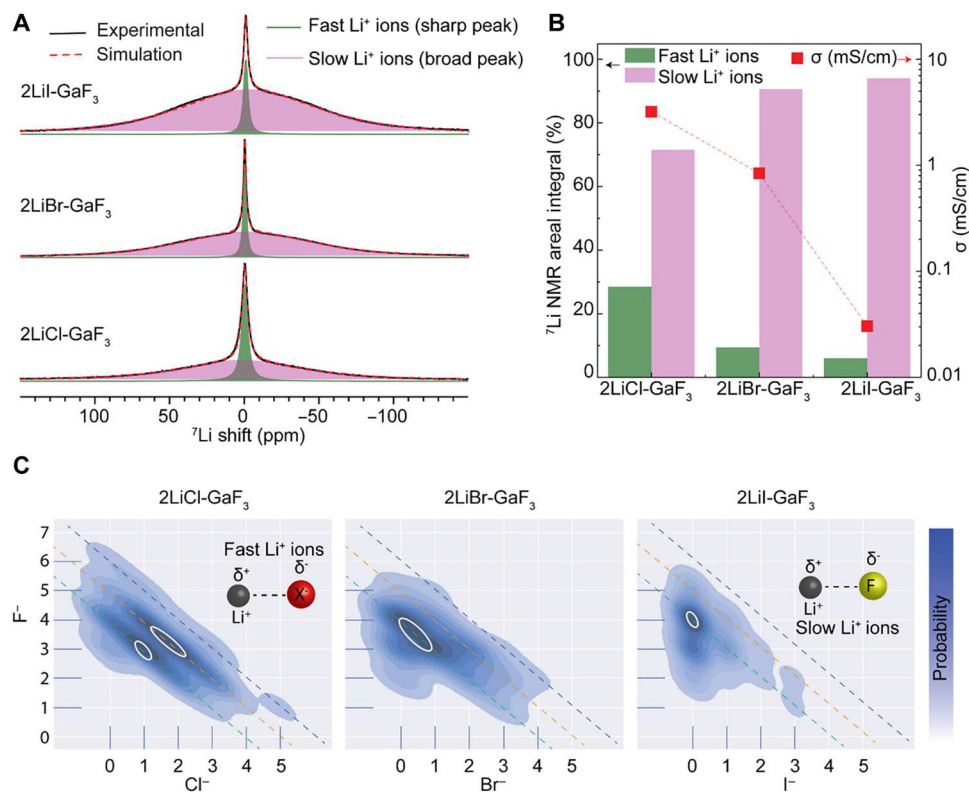
Li-ion dynamics in 2LiX-GaF$_3$ (X = Cl, Br, I)

Multinuclear solid-state NMR reveals that LiX and GaF$_3$ react to form complex mixed anions of Ga(F, X)$_n$. To understand the impact of this polyanion-constituted framework on the Li⁺ dynamics, ⁷Li NMR relaxometry is used. ⁷Li T_1 relaxation time is known to be correlated with the Li⁺-ion motional rate ($1/\tau_c$), according to Eq. 1 (44, 45) where γ is the gyromagnetic ratio, μ_o is permeability of vacuum, $\hbar$ is the reduced Planck constant, r_o is the interatomic

distance, and ω_o is the Larmor frequency.

$$\left(\frac{1}{T_1}\right) = \frac{3\mu_o^2\gamma^4\hbar^2}{10r_0^6}\left[\frac{\tau_c}{1 + (\omega_o\tau_c)^2} + \frac{4\tau_c}{1 + 4(\omega_o\tau_c)^2}\right] \quad (1)$$

Two motional regimes are depicted from Eq. 1, the fast-motional regime where $\omega_o\tau_c \ll 1$ and slow-motional regime where $\omega_o\tau_c \gg 1$. To determine the motional regime of Li⁺ ions, variable-temperature NMR relaxometry studies were conducted on the highly conductive 2LiCl-GaF$_3$ sample. Figure 6A shows the ⁷Li NMR spectra collected at temperatures between 25° and 95°C. While the resonances of the fast- and slow-moving Li components are both observed throughout the explored temperature range, increasing the temperature from 20° to 95°C involves converting slow-moving Li⁺ ions to fast-moving ones. The quantification of the NMR resonances is presented in Fig. 6B. We observe a progressive increase of the fraction of the fast-moving Li⁺ ions at the cost of the slow-moving ones, which plateaus at $T = 70$°C, suggesting an increase in the charge carrier concentration.

From variable-temperature T_1 relaxation measurements (Fig. 6C), we also observe that the increase in temperature does not cause significant changes in the T_1 relaxation of the resonance attributed to fast Li⁺ ions, whereas the relaxation time of the resonance from the slow Li⁺ ions decreases from 1.55 s at 25°C to 1.06 s at 95°C. This indicates that the two phases may be at different motional regimes of the Bloembergen-Purcell-Pound theory. The slow Li⁺ ions are in the slow motional regime where $\omega_o\tau_c \gg 1$, and shorter T_1 relaxation time depicts faster motion. The initial abnormal behavior of the T_1 of slow Li⁺ ions is likely due to phase transition below 40°C, echoing the electrochemical measurements shown in Fig. 2. The NMR resonance from the fast Li⁺ ions does not show significant changes in the T_1 relaxation time, suggesting that

Fig. 5. Analysis of Li local environments in 2LiX-GaF₃ (X = Cl, Br, I) with ⁷Li NMR and AIMD simulations. (**A**) ^{7}Li NMR spectra of 2LiX-GaF$_3$ exhibit two resonances: The sharp one comes from fast-moving Li$^+$ ions and the broad one is from slow-moving Li$^+$ ions. Li$^+$-ion dynamics are determined with NMR relaxometry shown in Fig. 6. (**B**) Quantification of the slow- and fast-moving Li$^+$ ions based on ^{7}Li NMR in (A). (**C**) Analysis of Li$^+$ coordination by F$^-$ and X$^-$ anions in the amorphous structure models for 2LiX-GaF$_3$ generated with AIMD simulated annealing.

the motion of these Li$^+$ ions lie in the intermediate region where $\omega_o\tau_c \approx 1$. High ionic conductivity at high temperature is attributed to the increased fraction of the fast Li$^+$-ion component (shorter T_1 relaxation time), i.e., increase in charge carrier concentration, as shown in Fig. 6C.

Further insights into the impact of the anion sublattice on the Li$^+$-ion dynamics can be obtained by comparing room-temperature ^{7}Li T_1 NMR relaxation times of 2LiX-GaF$_3$ (X = Cl, Br, I). Figure 7 shows the ^{7}Li T_1 relaxation times of the broad and sharp components in ^{7}Li NMR spectra of 2LiX-GaF$_3$ (X = Cl, Br, I). The fast-moving component is associated with a shorter T_1 relaxation time than the slow-moving component in all samples. 2LiCl-GaF$_3$ has the shortest T_1 relaxation time among all compositions suggesting the fastest Li motion, which correlates well with it having the highest ionic conductivity. It is worth mentioning that the T_1 data in Fig. 7 is acquired in an 11.7-T magnetic field (^{7}Li Larmor frequency ω_0, 194.3 MHz), which, as expected according to Eq. 1, results in slightly larger values than data reported in Fig. 6C, collected in a lower field of 7.0 T (^{7}Li Larmor frequency ω_0, 116.6 MHz).

DISCUSSION

Amorphous 2LiX-GaF$_3$ (X = Cl, Br, I) compounds are pliable fast Li$^+$ conductors, with ionic conductivities increasing from 0.03 mS/cm for 2LiI-GaF$_3$, to 0.84 mS/cm for 2LiBr-GaF$_3$, and up to 3.20 mS/cm for 2LiCl-GaF$_3$. In this work, we have combined

multinuclear solid-state NMR and DFT to characterize local structures and ion dynamics in these complex mixed-halide materials to understand the impact of composition on ionic conductivity.

^{71}Ga NMR experiments performed on all 2LiX-GaF$_3$ samples (Fig. 3A) reveal that Ga is mostly 3+. Moreover, the large C_q constant (>8 MHz) values indicate local disorder, which we ascribe to the existence of a wide variety of coordination environments around Ga, with coordination numbers ranging from $n = 4$ to $n = 6$. AIMD-generated amorphous structure models (Fig. 3, B and C) display considerable statistical variance in the Ga coordination of polyhedra GaX$_m$F$_{n-m}$ formed during the simulated annealing process. While Br$^-$ and I$^-$ form essentially one main type of GaX$_m$F$_{n-m}$ polyanion, with $n \approx 5$ ($m \approx 2$) and $n \approx 4$ ($m \approx 2$ to 3), respectively, the Cl$^-$-based compound is characterized by a multimodal distribution of Ga environments, with local maxima at $n \approx 4$ ($m \approx 3$), $n \approx 5$ ($m \approx 2$), and $n \approx 6$ ($m \approx 1$); see Fig. 3C. We also note that, despite the wide dispersion of the DFT calculated C_q values, C_q^{DFT} (table S1), average $\overline{C}_q^{DFT}$ calculated for GaX$_m$F$_{n-m}$ polyanions corresponding to the maxima outlined above are very close to the C_q values used for the experimental fitting (Table 1), namely, $\overline{C}_q^{DFT} = 12.6$ MHz ($n = 4, 5, 6$; $m = 1, 2, 3$) for 2LiCl-GaF$_3$; $\overline{C}_q^{DFT} = 11.7$ MHz ($n = 5$; $m = 2$) for 2LiBr-GaF$_3$; and $\overline{C}_q^{DFT} = 14.9$ MHz ($n = 4$; $m = 2$ to 3) for 2LiI-GaF$_3$.

The greater coordination flexibility of Ga in 2LiCl-GaF$_3$ may be attributed to two main factors. First, Cl$^-$ has a smaller ionic radius
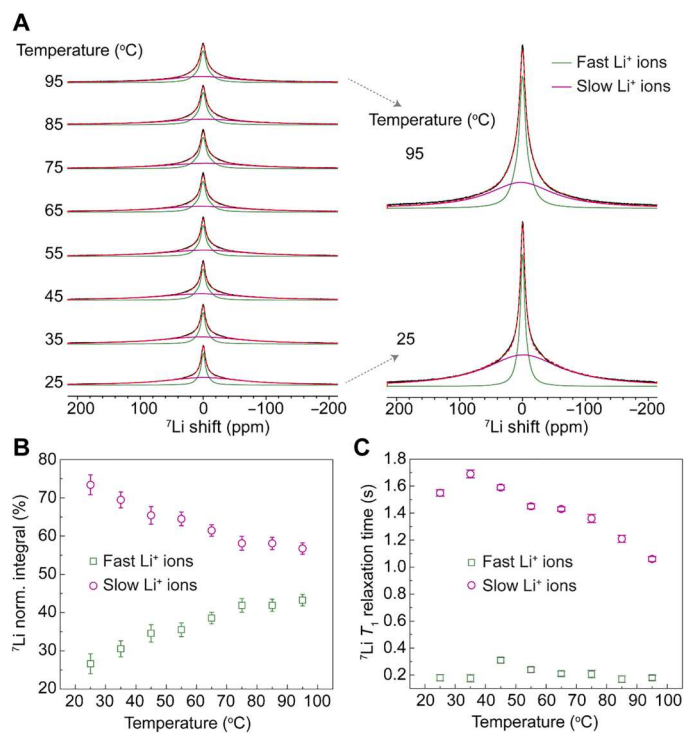
Fig. 6. Li⁺-ion dynamics of 2LiCl-GaF₃ probed with variable-temperature NMR lineshape analysis and relaxometry. (**A**) Variable-temperature static ^{7}Li NMR spectra, revealing that the resonances of the fast-moving and slow-moving Li⁺ ions adopt Lorentzian and Gaussian peak shapes, respectively. The Lorentzian line shape suggests fast relaxation induced by ion dynamics. (**B**) The quantified fractions of the fast- and slow-moving Li⁺ ions as a function of temperature obtained from the analysis of variable-temperature spectra in (A). (**C**) ^{7}Li NMR T_1 relaxation time measurements of 2LiCl-GaF₃ as a function of temperature.

Table 1. Quadrupole coupling constants C_q and η (asymmetry parameter) of ^{71}Ga NMR obtained for 2LiX-GaF₃ (X = Cl, Br, I) compounds both from experimental and computational methods. The computational C_q was derived by taking the average of the most common coordination types in 2LiCl-GaF₃, 2LiBr-GaF₃, and in 2LiI-GaF₃ in table S1, as found from the X and F distributions shown in Fig. 3C.

Samples	Experimental C_q (MHz)	η	Computational C_q (MHz)	η
2LiCl-GaF₃	8.8	0.61	12.6	0.7
2LiBr-GaF₃	8.0	0.65	11.7	0.7
2LiI-GaF₃	12.5	0.60	14.9	0.45

(1.81 Å) than Br⁻ (1.96 Å) and I⁻ (2.2 Å), which leaves room for a relatively larger number of both Cl⁻ and F⁻ ligands around Ga. Second, the electronegativity of Cl (3.16) is closer to that of F (3.98), which allows for a more homogeneous distribution of the electron density in mixed Ga(Cl, F)$_n$ polyanions and, therefore, for greater stability over a wide coordination range (n = 4, 5, 6), as demonstrated by the defect energies reported in table S2.

The complex Ga(X, F)$_n$ polyanions are further studied by examining the fluorine environment. On the basis of our DFT structure models, Ga(X, F)$_n$ polyanions are formed by partial substitution of F with X in the octahedral $[GaF_6]^{3-}$ building blocks of the GaF₃ precursor. Figure 3C shows that, in general, F is displaced from its original position relative to Ga to a greater extent when bigger X halides (I⁻ > Br⁻ > Cl⁻) are introduced. As fluorine is detached from its polar-covalent interaction with Ga, free F⁻ anions are released into the amorphous matrix. Hence, two different types of fluorine are outlined, namely, (i) F covalently bound to Ga in mixed polyanions Ga(X, F)$_n$ and (ii) free F⁻ anions with high mobility, as observed in ^{19}F NMR (Fig. 4, A to C). Single F⁻ anions are expected to have higher mobility compared to relatively large polyanions such as Ga(X, F)$_n$. Moreover, the increasing intensity of the ^{19}F NMR narrow peak (full width at half maximum <1 kHz) from fast-moving F in the 2LiBr-GaF₃ and 2LiI-GaF₃ samples, correlates with the increasing amount of free F⁻ anions in the corresponding structural models, thus supporting this interpretation. The ^{19}F NMR signals integration in Fig. 4C, reveals that more than 80% of F in 2LiI-GaF₃ is mobile and does not participate in the formation of Ga(X, F)$_n$ polyanions.

In contrast to the increasing amount of fast-moving F observed in ^{19}F NMR, ^{7}Li NMR reveals that the amount of mobile Li decreases with X varying from Cl to Br and I. The sharp ^{7}Li NMR signal from fast-moving Li ions in 2LiI-GaF₃ is reduced to about one-third of that observed in 2LiCl-GaF₃ (Fig. 5, A and B). This demonstrates that the formation of complex Ga(X, F)$_n$ polyanions has a substantial impact on the lithium chemical environment and, consequently, on the Li⁺ mobility. Once again, further insight can be achieved by inspecting the Li(X, F) local structures formed in the amorphous models generated by simulated annealing. In this case, a clear correspondence emerges between the intensification of the ^{7}Li NMR signal from slow-moving Li (and parallel decrease of the fast-moving Li component) observed as X changes from Cl to Br and to I, and the prevalence of F⁻ [over Ga(X, F)$_n$ polyanions] as the counterion around Li⁺. It is noteworthy that the Li⁺ environment is ultimately shaped by the variety of mixed-halide polyanions formed around Ga, which drive the short-range ordering constituting the amorphous framework of 2LiX-GaF₃ compounds.

Variable-temperature ^{7}Li NMR of 2LiCl-GaF₃ deciphers the transition of slow-moving Li to the fast-moving Li phase as shown in Fig. 6B. We thereby conclude that the more Li⁺ is engaged in strong ionic interactions with highly electronegative free F⁻ anions, the more the Li⁺ mobility in 2LiX-GaF₃ compounds is hindered. This feature lastly explains the lower ionic conductivity of the 2LiBr-GaF₃ and 2LiI-GaF₃ compounds compared to 2LiCl-GaF₃. The involvement of fluorine in the constitutive polyanionic framework of the latter limits the binding effect of F⁻ anions on the charge carriers, thus providing Li⁺ with more freedom to diffuse through the amorphous medium.

Conclusion and perspectives
The present work elucidates local structures in amorphous 2LiX-GaF₃ (X = Cl, Br, I) electrolytes and determines the origin of high ionic conductivity via a combined approach of advanced solid-state NMR characterizations and DFT calculations. High-energy mechanochemical mixing of binary lithium halides LiX with GaF₃ results in the formation of complex anions Ga(X, F)$_n$. A larger variety of GaX$_m$F$_{n-m}$ coordination polyhedra are formed in accommodating
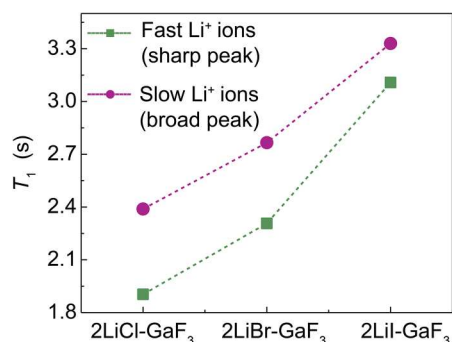
Fig. 7. Li$^+$-ion dynamics of 2LiX-GaF$_3$ (X = Cl, Br, I) probed with NMR relaxometry. Room-temperature ^{7}Li NMR T_1 relaxation times of the slow and fast-moving components in 2LiX-GaF$_3$ (X = Cl, Br, I).

X = Cl along with F, as opposed to X = Br or I. The F involvement in forming GaX$_m$F$_{n-m}$ polyanions is beneficial for fast Li$^+$ ion conduction due to consequent diversification of the Li environment avoiding exclusive Li-F ionic interactions. The clustering of the halides on gallium-based polyanions weakens the Li$^+$ binding affinity of the negative host enabling fast ion transport.

This study introduces a novel concept of charge clustering for electrolyte design, broadly relevant to liquid-, polymer-, and ceramic/glass-type ion conductors. Therefore, we expect that this work will inspire new frontiers for electrolyte research beyond using simple monoanions or polyanions, which could potentially produce electrolytes with performance far exceeding state-of-the-art. Specifically, in the case of amorphous 2LiX-GaF$_3$ electrolytes, this strategy also affords the employment of halide elements to enhance the electrochemical stability without introducing strong Li-halide interactions. Last, we note that the phenomenon of charge clustering on Ga(X,F)$_n$ polyanions, which weakens the cation binding, is analogous to a phenomenon recently observed in biological systems, i.e., clustering of carboxylate (COO$^-$) groups on proteins that significantly alters their binding to Ca^{2+} and Mg^{2+} (24). Therefore, our findings may also help to design multivalent (Ca^{2+} and Mg^{2+}) ion conductors, a currently challenging area of research, and will generate broader and high impacts if successful.

MATERIALS AND METHODS
Synthesis of 2LiX-GaF$_3$ (X = Cl, Br, I)
The materials were prepared by planetary milling (Pulverisette 7 PL; Fritsch) using as-received LiCl (99%; Sigma-Aldrich), LiBr (≥99%; Sigma-Aldrich), LiI (99.9%; Sigma-Aldrich), and GaF$_3$ (99.85%; Alfa Aesar) in the same way as described in our previous work.[23] LiX/GaF$_3$ (2/1, mol/mol) were placed into a silicon nitride container that was sealed in an Ar-filled glove box to minimize air exposure during the mechanochemical synthesis. The powders were mixed at 700 rpm for 10 min, followed by 5-min rest, and this mixing and rest procedure was repeated 72 times, resulting in a clay-like compound.

X-ray diffraction
"Clay-like" samples were packed in a zero-background XRD sample holder that was covered with a polyimide Kapton film to minimize sample exposure to humid air. XRD was performed using a Rigaku

D8 powder diffractometer with the Bragg-Brentano geometry at a voltage of 44 kV and a current of 40 mA with Cu-Kα radiation (λ = 1.5406 Å). The data were collected in the 2Θ range of 10° to 80° at a step size of 0.03° with a total acquisition time of 30 min.

Electrochemical analysis
The ionic conductivity was determined using EIS (EIS, Solartron Analytical, UK). EIS was performed using the cell confirmation of stainless steel/2LiX-GaF$_3$/stainless steel in the frequency range from 1 MHz to 0.1 Hz and a temperature range of 20° to 80°C.

Solid-state NMR
^{7}Li (spin-3/2) and ^{19}F (spin-1/2) solid-state NMR experiments were performed using a Bruker Avance-III 500 MHz (11.7 T) spectrometer at Larmor frequencies of 194.4 and 470 MHz, respectively. Experiments were carried out under static conditions, as the clay-like nature of the samples made them unsuitable for magic-angle-spinning (MAS) NMR experiments. Single-pulse ^{7}Li NMR experiments were performed with a π/2 pulse length of 3.1 μs and a recycle delay of 20 s. For ^{19}F NMR, a static spin-echo sequence was used with a π/2 pulse length of 4.4 μs and a recycle delay of 50 s. ^{71}Ga (spin-3/2) NMR was performed on an 830 MHz (19.6 T) spectrometer at the Larmor frequency of 253 MHz. A static QCPMG pulse sequence with a π/2 pulse length of 2 μs was used to acquire the ^{71}Ga NMR spectra. Variable-temperature ^{7}Li NMR spectroscopy and relaxometry measurements on 2LiCl-GaF$_3$ were conducted to determine Li$^+$-ion dynamics using a Bruker 300 MHz (7.05-T) spectrometer at the Larmor frequency of 116 MHz, and a 4-mm Bruker MAS NMR probe at an 8-kHz spinning rate. The inversion recovery pulse sequence was used to determine ^{7}Li T_1 relaxation times, with a π/2 pulse length of 2.5 μs. The spectra were collected between 25° and 95°C with increments of every 10°C and the sample was allowed to equilibrate for 10 min at each temperature. All ^{7}Li spectra were calibrated using LiCl(s) at −1.1 ppm and ^{19}F NMR using LiF(s) at −203 ppm. ^{71}Ga NMR was calibrated using GaF$_3$(s) at 0 ppm.

Computational
Simulated annealing
Amorphous 2LiX-GaF$_3$ (X = Cl, Br, and I) structure models were generated via AIMD simulated annealing followed by structure relaxation performed with the Vienna Ab initio Simulation Package (VASP) (46). Projector-augmented wave potentials were used within the generalized gradient approximation of the density functional in its Perdew-Burke-Ernzerhof formulation (47, 48). AIMD simulations were carried out at the Γ-point only, using the largest default kinetic energy cutoff of constituent elements. The AIMD time step was set to 1 to 2 fs, and the temperature was controlled by periodic velocity rescaling every 50 or 100 steps. Following (49–50), initial atomic configurations were built in cubic volumes using the packing optimization procedure developed in Packmol (51). These atomic configurations (unit cells with 120 atoms each) were used as high-temperature (1000 to 2000 K) structure guesses to which a descending temperature ramp was applied at a cooling rate of 100 K/ps, discontinued by equilibration steps of at least 10 ps. All AIMD simulations were performed at constant volume, and the latter was resized isotropically (i.e., by variations of ±0.1 Å along each Cartesian direction) at intervals during the equilibration to counterbalance the calculated total pressure. Structure

optimizations following the cooling process were performed using the higher-accuracy DFT settings of the Materials Project (*52*). Atomic charges were calculated using Henkelman *et al.*'s (*53*) algorithm for Bader decomposition of charge density (*54*). Local structures and coordination environments were analyzed using the CrystalNN near-neighbor finding algorithm implemented in the python library pymatgen (*55*, *56*). For 3D visualization of the amorphous structure models, we used VESTA (*57*).

NMR calculations

The optimized amorphous structures generated by simulated annealing were used for calculations of NMR tensors using the Gauge Including Projector Augmented Waves method (*9*, *11*). The energy cutoff was set to 600 eV, and a k-point grid density of at least 500 per reciprocal atom was guaranteed. A threshold for convergence on the electronic energy of 10^{-8} eV was used to ensure high accuracy. Calibration factors (+90 ppm for ^{71}Ga shifts and +15 ppm for ^{19}F shifts) were obtained on the basis of calculated and experimental shifts of model compounds GaF_3 (*11*). Electric field gradient tensors were calculated to determine the quadrupole coupling constant (C_q) (*12*). The nuclear quadrupole moment (Q) of ^{71}Ga was set to 107 mb for the calculation of C_q (*14*).

Supplementary Materials

This PDF file includes:
Fig. S1
Tables S1 and S2

REFERENCES AND NOTES

1. J. Janek, W. G. Zeier, A solid future for battery development. *Nat. Energy* **1**, 16141 (2016).
2. A. Manthiram, X. Yu, S. Wang, Lithium battery chemistries enabled by solid-state electrolytes. *Nat. Rev. Mater.* **2**, 16103 (2017).
3. A. M. Abakumov, S. S. Fedotov, E. V. Antipov, J.-M. Tarascon, Solid state chemistry for developing better metal-ion batteries. *Nat. Commun.* **11**, 4976 (2020).
4. J. C. Bachman, S. Muy, A. Grimaud, H.-H. Chang, N. Pour, S. F. Lux, O. Paschos, F. Maglia, S. Lupart, P. Lamp, L. Giordano, Y. Shao-Horn, Inorganic solid-state electrolytes for lithium batteries: Mechanisms and properties governing ion conduction. *Chem. Rev.* **116**, 140–162 (2016).
5. Y. Kato, S. Hori, T. Saito, K. Suzuki, M. Hirayama, A. Mitsui, M. Yonemura, H. Iba, R. Kanno, High-power all-solid-state batteries using sulfide superionic conductors. *Nat. Energy* **1**, 16030 (2016).
6. P. Adeli, J. D. Bazak, K. H. Park, I. Kochetkov, A. Huq, G. R. Goward, L. F. Nazar, Boosting solid-state diffusivity and conductivity in lithium superionic argyrodites by halide substitution. *Angew. Chem. Int. Ed.* **58**, 8681–8686 (2019).
7. S. V. Patel, S. Banerjee, H. Liu, P. Wang, P.-H. Chien, X. Feng, J. Liu, S. P. Ong, Y.-Y. Hu, Tunable lithium-ion transport in mixed-halide argyrodites Li$_6$–XPS$_5$–XClBr$_x$: An unusual compositional space. *Chem. Mater.* **33**, 1435–1443 (2021).
8. M. A. Kraft, S. Ohno, T. Zinkevich, R. Koerver, S. P. Culver, T. Fuchs, A. Senyshyn, S. Indris, B. J. Morgan, W. G. Zeier, Inducing high ionic conductivity in the lithium superionic argyrodites Li$_{6+x}$P$_{1-x}$Ge$_x$S$_5$I for all-solid-state batteries. *J. Am. Chem. Soc.* **140**, 16330–16339 (2018).
9. X. Feng, P.-H. Chien, Y. Wang, S. Patel, P. Wang, H. Liu, M. Immediato-Scuotto, Y.-Y. Hu, Enhanced ion conduction by enforcing structural disorder in Li-deficient argyrodites Li$_{6-x}$PS$_{5-x}$Cl$_{1+x}$. *Energy Storage Mater.* **30**, 67–73 (2020).
10. P. Wang, S. Patel, H. Liu, P.-H. Chien, X. Feng, L. Gao, B. Chen, J. Liu, Y.-Y. Hu, Configurational and dynamical heterogeneity in superionic Li$_{5.3}$PS$_{4.3}$Cl$_{1.7-x}$Br$_x$. *Adv. Funct. Mater.* 2307954, (2023).
11. L. Nazar, P. Adeli, J.D. Bazak, K.-H. Park, I. Kochetkov, A. Huq, G. Goward, Boosting Solid-State Diffusivity and Conductivity in Lithium Superionic Argyrodites by Halide Substitution, *Angewandte Chemie International Edition 0* (ja).
12. R. Murugan, V. Thangadurai, W. Weppner, Fast lithium ion conduction in garnet-type Li$_7$La$_3$Zr$_2$O$_{12}$. *Angew. Chem. Int. Ed.* **46**, 7778–7781 (2007).
13. E. A. Wu, S. Banerjee, H. Tang, P. M. Richardson, J.-M. Doux, J. Qi, Z. Zhu, A. Grenier, Y. Li, E. Zhao, G. Deysher, E. Sebti, H. Nguyen, R. Stephens, G. Verbist, K. W. Chapman, R. J. Clément, A. Banerjee, Y. S. Meng, S. P. Ong, A stable cathode-solid electrolyte composite for high-voltage, long-cycle-life solid-state sodium-ion batteries. *Nat. Commun.* **12**, 1256 (2021).
14. Y. Xiao, Y. Wang, S.-H. Bo, J. C. Kim, L. J. Miara, G. Ceder, Understanding interface stability in solid-state batteries. *Nat. Rev. Mater.* **5**, 105–126 (2020).
15. A. Banerjee, X. Wang, C. Fang, E. A. Wu, Y. S. Meng, Interfaces and interphases in all-solid-state batteries with inorganic solid electrolytes. *Chem. Rev.* **120**, 6878–6933 (2020).
16. Z. Ding, J. Li, J. Li, C. An, Review—Interfaces: Key issue to be solved for all solid-state lithium battery technologies. *J. Electrochem. Soc.* **167**, 070541 (2020).
17. H. Huo, J. Gao, N. Zhao, D. Zhang, N. G. Holmes, X. Li, Y. Sun, J. Fu, R. Li, X. Guo, X. Sun, A flexible electron-blocking interfacial shield for dendrite-free solid lithium metal batteries. *Nat. Commun.* **12**, 176 (2021).
18. M. Cronau, M. Szabo, C. König, T. B. Wassermann, B. Roling, How to measure a reliable ionic conductivity? The stack pressure dilemma of microcrystalline sulfide-based solid electrolytes. *ACS Energy Lett.* **6**, 3072–3077 (2021).
19. J.-M. Doux, Y. Yang, D.H.S. Tan, H. Nguyen, E.A. Wu, X. Wang, A. Banerjee, Y.S. Meng, Pressure effects on sulfide electrolytes for all solid-state batteries. *J. Mater. Chem. A* **8**, 5049–5055 (2020).
20. P. Minnmann, F. Strauss, A. Bielefeld, R. Ruess, P. Adelhelm, S. Burkhardt, S. L. Dreyer, E. Trevisanello, H. Ehrenberg, T. Brezesinski, F. H. Richter, J. Janek, Designing cathodes and cathode active materials for solid-state batteries. *Adv. Energy Mater.* **12**, 2201425 (2022).
21. Y. Choo, Y. Hwa, E.J. Cairns, A review of the rational interfacial designs and characterizations for solid-state lithium/sulfur cells. *Electrochemical Science Advances* **2**, e2100154 (2022).
22. S. R. Combs, P. K. Todd, P. Gorai, A. E. Maughan, Editors' choice—review—designing defects and diffusion through substitutions in metal halide solid electrolytes. *J. Electrochem. Soc.* **4**, 040551 (2022).
23. S.-K. Jung, H. Gwon, G. Yoon, L. J. Miara, V. Lacivita, J.-S. Kim, Pliable lithium superionic conductor for all-solid-state batteries. *ACS Energy Lett.* **6**, 2006–2015 (2021).
24. T. Sörensen, S. Leeb, J. Danielsson, M. Oliveberg, Polyanions cause protein destabilization similar to that in live cells. *Biochemistry* **60**, 735–746 (2021).
25. C. A. Angell, K. L. Ngai, G. B. McKenna, P. F. McMillan, S. W. Martin, Relaxation in glass-forming liquids and amorphous solids. *J. Appl. Phys.* **88**, 3113–3157 (2000).
26. M. Aniya, M. Ikeda, A model for non-arrhenius ionic conductivity. *Nanomaterials* **9**, 911 (2019).
27. M. D. Ingram, C. A. Vincent, A. R. Wandless, Temperature dependence of ionic conductivity in glass: Non-arrhenius behavior in the Ag$_7$I$_4$AsO$_4$ system. *J. Non Cryst. Solids* **53**, 73–82 (1982).
28. X. Li, J. Liang, X. Yang, K. R. Adair, C. Wang, F. Zhao, X. Sun, Progress and perspectives on halide lithium conductors for all-solid-state lithium batteries. *Energ. Environ. Sci.* **13**, 1429–1461 (2020).
29. B. Zhang, J. Zhong, Y. Zhang, L. Yang, J. Yang, S. Li, L.-W. Wang, F. Pan, Z. Lin, Discovering a new class of fluoride solid-electrolyte materials via screening the structural property of Li-Ion sublattice. *Nano Energy* **79**, 105407 (2021).
30. Y. Tomita, H. Ohki, K. Yamada, T. Okuda, Ionic conductivity and structure of halocomplex salts of group 13 elements. *Solid State Ion.* **136-137**, 351–355 (2000).
31. R. P. Chapman, D. L. Bryce, Application of multinuclear magnetic resonance and gauge-including projector-augmented-wave calculations to the study of solid group 13 chlorides. *Phys. Chem. Chem. Phys.* **11**, 6987–6998 (2009).
32. J. T. Ash, P. J. Grandinetti, Solid-state NMR characterization of ^{69}Ga and ^{71}Ga in crystalline solids. *Magn. Reson. Chem.* **44**, 823–831 (2006).
33. F. A. Perras, D. L. Bryce, Direct characterization of metal–metal bonds between nuclei with strong quadrupolar interactions via NMR spectroscopy. *J. Phys. Chem. Lett.* **5**, 4049–4054 (2014).
34. H. Tanaka, A. Kobayashi, T. Saito, K. Kawano, T. Naito, F. H. Kobayashi, λ-type BETS salts containing a mixed halide gallium anion, GaX$_x$Y$_{4-x}$⊖ [X, Y = F, Cl, Br; BETS = Bis(Ethylenedithio)tetraselenafulvalene]. *Adv. Mater.* **8**, 812–815 (1996).
35. B. R. McGarvey, M. J. Taylor, D. G. Tuck, Gallium-71 NMR studies of anionic gallium halide species in nonaqueous solution. *Inorg. Chem.* **20**, 2010–2013 (1981).
36. G. Davidson, Elements of group 3. *Coord. Chem. Rev.* **49**, 117–192 (1983).
37. D. Massiot, T. Vosegaard, N. Magneron, D. Trumeau, V. Montouillout, P. Berthet, T. Loiseau, B. Bujoli, ^{71}GaNMR of reference GaIV, GaV, and GaVI compounds by MAS and QPASS, extension of gallium/aluminum NMR parameter correlation. *Solid State Nucl. Magn. Reson.* **15**, 159–169 (1999).
38. M. Kumar, K. Yamada, T. Okuda, S. S. Sekhon, Temperature dependence of ^{19}F NMR and ion transport parameters of fluoride ion conductors SnF$_2$—PbF$_2$ and 2SnF$_2$—NH$_4$F prepared by mechanical milling. *Phys. Status Solidi B* **239**, 432–438 (2003).
39. F. Wang, C. P. Grey, A 1- and 2-D ^{19}F MAS NMR study of fluoride-ion mobility in α PbF$_2$. *J. Am. Chem. Soc.* **120**, 970–980 (1998).

40. F. Preishuber-Pflügl, P. Bottke, V. Pregartner, B. Bitschnau, M. Wilkening, Correlated fluorine diffusion and ionic conduction in the nanocrystalline F− solid electrolyte $Ba_{0.6}La_{0.4}F_{2.4}$ —^{19}F T1(ρ) NMR relaxation vs. conductivity measurements. *Phys. Chem. Chem. Phys.* **16**, 9580–9590 (2014).

41. Y. Liu, L. Hong, R. Jiang, Y. Wang, S. V. Patel, X. Feng, H. Xiang, Multifunctional electrolyte additive stabilizes electrode–electrolyte interface layers for high-voltage lithium metal batteries. *ACS Appl. Mater. Interfaces* **13**, 57430–57441 (2021).

42. P. Heitjans, M. Wilkening, Ion dynamics at interfaces: Nuclear magnetic resonance studies. *MRS Bulletin* **34**, 915–922 (2009).

43. F. Preishuber-Pflügl, M. Wilkening, Mechanochemically synthesized fluorides: Local structures and ion transport. *Dalton Trans.* **45**, 8675–8687 (2016).

44. N. Bloembergen, E. M. Purcell, R. V. Pound, Relaxation effects in nuclear magnetic resonance absorption. *Phys. Rev.* **73**, 679–712 (1948).

45. I. Hanghofer, M. Brinek, S. L. Eisbacher, B. Bitschnau, M. Volck, V. Hennige, I. Hanzu, D. Rettenwander, H. M. R. Wilkening, Substitutional Disorder: Structure and ion dynamics of the argyrodites Li_6PS_5Cl, Li_6PS_5Br and Li_6PS_5I. *Phys. Chem. Chem. Phys.* **21**, 8489–8507 (2019).

46. G. Kresse, J. Furthmüller, Efficient iterative schemes for ab initio total-energy calculations using a plane-wave basis set. *Phys. Rev. B Condens. Matter.* **54**, 11169–11186 (1996).

47. P. E. Blöchl, Projector augmented-wave method. *Phys. Rev. B Condens. Matter.* **50**, 17953–17979 (1994).

48. J. P. Perdew, K. Burke, M. Ernzerhof, Generalized gradient approximation made simple. *Phys. Rev. Lett.* **77**, 3865–3868 (1996).

49. V. Lacivita, A. S. Westover, A. Kercher, N. D. Phillip, G. Yang, G. Veith, G. Ceder, N. J. Dudney, Resolving the amorphous structure of lithium phosphorus oxynitride (lipon). *J. Am. Chem. Soc.* **140**, 11029–11038 (2018).

50. V. Lacivita, N. Artrith, G. Ceder, Structural and compositional factors that control the Li-Ion conductivity in LiPON electrolytes. *Chem. Mater.* **30**, 7077–7090 (2018).

51. L. Martínez, R. Andrade, E. G. Birgin, J. M. Martínez, PACKMOL: A package for building initial configurations for molecular dynamics simulations. *J. Comput. Chem.* **30**, 2157–2164 (2009).

52. A. Jain, S. P. Ong, G. Hautier, W. Chen, W. D. Richards, S. Dacek, S. Cholia, D. Gunter, D. Skinner, G. Ceder, K. A. Persson, Commentary: The materials project: A materials genome approach to accelerating materials innovation. *APL Mater.* **1**, 011002 (2013).

53. G. Henkelman, A. Arnaldsson, H. Jónsson, A fast and robust algorithm for bader decomposition of charge density. *Comput. Mater. Sci.* **36**, 354–360 (2006).

54. W. Tang, E. Sanville, G. Henkelman, A grid-based bader analysis algorithm without lattice bias. *J. Phys. Condens. Matter* **21**, 084204 (2009).

55. H. Pan, A. M. Ganose, M. Horton, M. Aykol, K. A. Persson, N. E. R. Zimmermann, A. Jain, Benchmarking coordination number prediction algorithms on inorganic crystal structures. *Inorg. Chem.* **60**, 1590–1603 (2021).

56. S. P. Ong, W. D. Richards, A. Jain, G. Hautier, M. Kocher, S. Cholia, D. Gunter, V. L. Chevrier, K. A. Persson, G. Ceder, Python Materials Genomics (Pymatgen): A robust, open-source python library for materials analysis. *Comput. Mater. Sci.* **68**, 314–319 (2013).

57. K. Momma, F. Izumi, VESTA 3 for three-dimensional visualization of crystal, volumetric and morphology data. *J. Appl. Cryst.* **44**, 1272–1276 (2011).